University Library



A gateway to Melbourne's research publications

Minerva Access is the Institutional Repository of The University of Melbourne

Author/s:
Turpin, A;McKendrick, AM

Title:
Improving Personalized Structure to Function Mapping From Optic Nerve Head to Visual Field.

Date:
2021-01-08

Citation:
Turpin, A. & McKendrick, A. M. (2021). Improving Personalized Structure to Function Mapping From Optic Nerve Head to Visual Field.. Translational Vision Science and Technology, 10 (1), https://doi.org/10.1167/tvst.10.1.19.

Persistent Link:
https://hdl.handle.net/11343/272792

License:
CC BY-NC-ND

tvst

Article

Improving Personalized Structure to Function Mapping From Optic Nerve Head to Visual Field

Andrew Turpin[1] **and Allison M. McKendrick**[2]

[1] School of Computing & Information Systems, The University of Melbourne, Melbourne, Australia
[2] Department of Optometry & Vision Sciences, The University of Melbourne, Melbourne, Australia

Correspondence: Andrew Turpin, School of Computing & Information Systems, The University of Melbourne, Parkville, Victoria, 3010, Australia.
e-mail: aturpin@unimelb.edu.au

Received: July 1, 2020
Accepted: November 21, 2020
Published: January 8, 2021

Keywords: glaucoma; visual field; perimetry; optical coherence tomography; structure-function; mapping

Citation: Turpin A, McKendrick AM. Improving personalized structure to function mapping from optic nerve head to visual field. Trans Vis Sci Tech. 2021;10(1):19, https://doi.org/10.1167/tvst.10.1.19

Purpose: Maps are required to relate visual field locations to optic nerve head regions. We compare individualized structure-to-function mapping (CUSTOM-MAP) to a population-derived mapping schema (POP-MAP).

Methods: Maps were compared for 118 eyes with glaucomatous field loss, circumpapillary retinal nerve fiber layer (cpRNFL) thickness measured using spectral domain optical coherence tomography (OCT), and two landmarks: the optic nerve head (ONH) position relative to the fovea and the temporal raphe angle. Locations with visual field damage (total deviation < -6 dB) were mapped to 30° ONH sectors centered on the angle given by each mapping schema. The concordance between damaged function and damaged structure was determined per location for various cpRNFL damage probability levels, with the number of concordant locations divided by the total number of damaged field locations providing a concordance ratio per eye.

Results: For the strictest concordance criteria (minimum cpRNFL thickness $<$ 1% of normal), CUSTOM-MAP had higher mean concordance ratio than POP-MAP (60.5% c.f. 57.0% paired Wilcoxon, $P = 0.005$), with CUSTOM-MAP having a higher ratio in 43 eyes and POP-MAP having a higher ratio in 21 eyes. For all cpRNFL probability levels $<$20% of normal, more locations concorded for CUSTOM-MAP than POP-MAP. Inspection of the spatial patterns of differences revealed that CUSTOM-MAP often performed better in the arcuate regions, whereas POP-MAP had benefits inferior to the macula.

Conclusions: Anatomic parameters required for individualized structure-function mapping are readily measured with OCT and can provide improved concordance for some eyes.

Translational Relevance: Personalizing structure-function mapping may improve concordance between these measures. We provide a web-based tool for creating customized maps.

Introduction

Estimates of visual field sensitivity and retinal nerve fiber layer thickness assessment are both essential for modern diagnosis and management of glaucoma. Despite significant advances in technology directed to glaucoma diagnosis and management, in a clinical setting these measures are typically derived separately and often qualitatively compared. In recent years, a range of more sophisticated approaches for combining information from retinal structure and visual function have been suggested, such as using the structural data to seed visual field testing[1,2] or combining the information from both tools into single indexes of damage.[3,4] Such applications (including routine clinical care) require spatial mapping between visual field space and relevant regions of interest on clinical imaging.[5] This article focuses on the problem of mapping peripapillary regions to visual field locations and updates our previous approach to custom mapping, taking into account newly available clinical data.

The most commonly used map from locations in visual field space to positions on the optic nerve head (ONH) or peripapillary retinal nerve fiber layer (RNFL) is that of Garway-Heath et al.,[6,7] which

Copyright 2021 The Authors

This work is licensed under a Creative Commons Attribution-NonCommercial-NoDerivatives 4.0 International License.

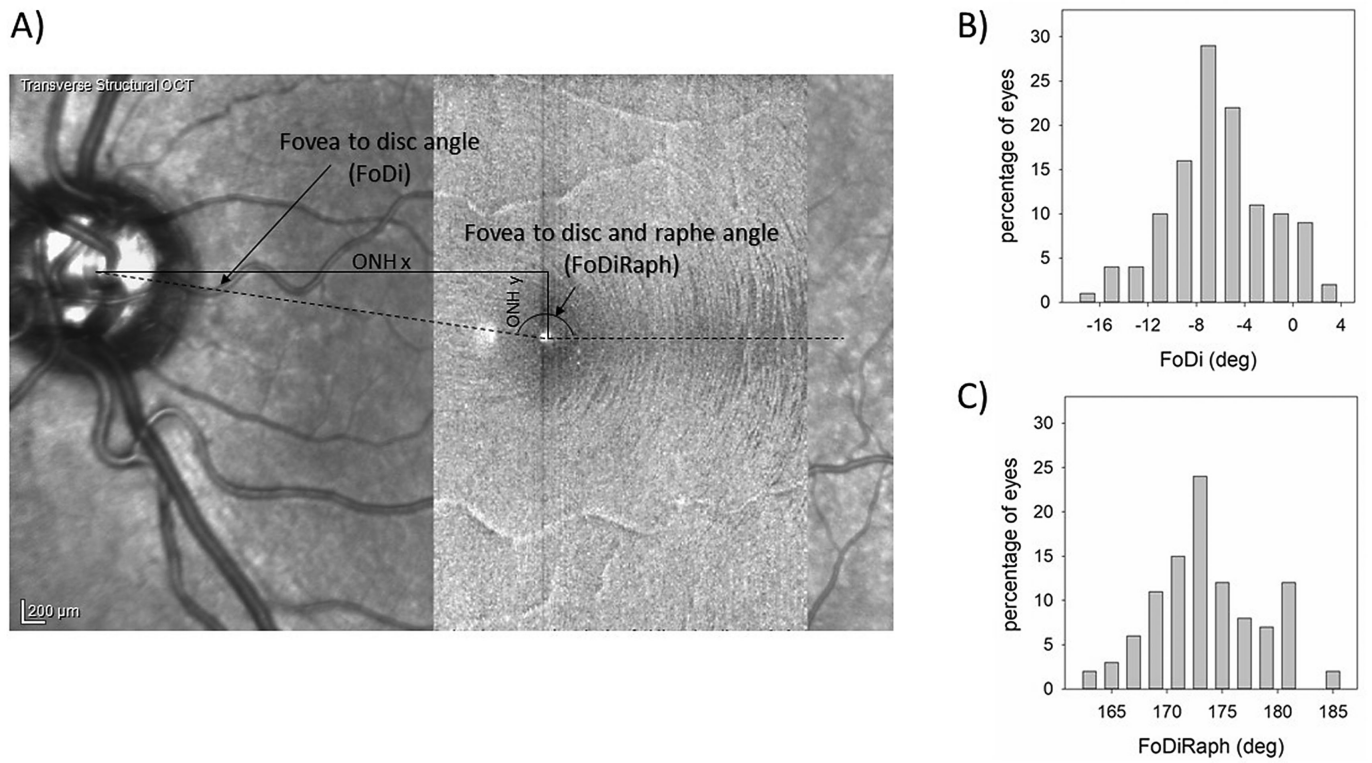


Figure 1. (**A**) Illustration of the relevant landmarks for individual structure-function mapping, and distribution of the same in our empirical dataset. Landmarks are superimposed on an en-face image of a left eye. The right-hand area of the image is a high-resolution transverse section, enabling visualization of the temporal raphe. ONHX and ONHY are the x and y coordinates of the optic nerve head relative to the fovea. (**B**) The distribution of fovea-to-disc angles in our dataset. (**C**) The distribution of fovea-disc-raphe angles in our dataset.

divides the ONH into 6 sectors, and the central 30 degrees of the visual field into 6 corresponding regions. The Garway-Heath map has been incorporated in numerous commercially available devices and was originally derived from hand-tracing of retinal photographs of 69 people with established normal tension glaucoma leading to retinal nerve fiber bundle defects that were visible by eye.

While readily interpretable, a drawback of typical implementations of the Garway-Heath map[6,7] is that it is based on anatomic population averages and is spatially very coarse, restricting the mapping of visual field locations to one of only six sectors (although more specific point-wise mapping to the 24-2 test pattern is presented within the author's original publication). A more fine-grained map was developed by Jansonius et al.,[8,9] where the axon trajectory of any location in the central visual field can be produced and insertion points into the optic nerve head can range over the full circumpapillary 360° possible. The Jansonius model was derived from a series of 83 eyes (55 in the 2009 article[8] and 28 in the 2012 article[9]), with the final model designed to represent a population average.

Although population average anatomy models are easy to apply, there are several key anatomic features that show marked variation in normal eyes that should result in significant deviations from the average map in some people.[10] One of these features is the position of the temporal raphe. With the advent of ultra-high–resolution OCT, it is now well established that temporal raphe position varies significantly within the population.[11–14] A second relevant feature is the position of the optic nerve head relative to the fovea, which also shows significant population variance.[13,15] Figure 1A illustrates these features.

We have previously published a model for deriving individualized structure function maps[16,17] that bears some in-principal similarity to the approach of Carreras et al.[18] The basic principle of these models is that retinal ganglion cell axons should seek to take the shortest path possible across the retina to the optic nerve head but should also avoid the foveal region. Here, we explore the differences that arise between our individualized mapping and the population-based map of Jansonius et al.,[9] using an empirical visual field and OCT dataset. This empirical data has the following: (1) established visual field damage,

(2) measurement of the position of the raphe, and (3) measurement of the optic nerve head position. Advances in imaging technology since our original mapping publication have enabled the availability of such empirical data. In an attempt to measure whether our map is more effective than the population-based approach, we compare the correspondence between visual field damage and OCT damage as predicted by our mapping scheme and that of Jansonious et al.[9] across the dataset and illustrate key differences with case examples.

Methods

Empirical Data

Visual field data were selected retrospectively from participants with glaucoma who had previously contributed to research projects in our laboratory. This research followed the tenets of the Declaration of Helsinki. Informed consent was acquired from the participants at the time of data collection using protocols approved by the University of Melbourne Human Research Ethics committee [ID1544011; ID 1646955]. General inclusion criteria were best corrected visual acuity of 6/9 or better; refractive error of less than 8 D spherical, and no more than 2 D of astigmatism; absence of systemic diseases or medications that could affect the visual field or the ability to take a perimetric test. All participants had a confirmed ophthalmological diagnosis of primary open angle glaucoma. Significant age-related lens change (>NC 1.5 as classified using LOCS III)[19] was also an exclusion criteria.

For the current analytical study, eyes were selected on the basis of visual fields alone, with the requirement for visual fields to have no more than 20% false-positive results, 20% false-negative results, and 20% fixation losses and to have established visual field loss with at least one location in the visual field with a total deviation of less than −6 dB. Visual fields were also required to have a spatial pattern of visual field loss consistent with typical patterns of loss associated with glaucoma. In total, 118 eyes from 72 individuals were included (age 57–81 years: mean 71 years, SD = 6.5 years). A histogram of the distributions of mean deviation and pattern standard deviation is shown in Figure 2.

Circumpapillary RNFL (cpRNFL) data were available for same day of testing as the visual field data for 107 eyes, and within three weeks for the remainder. Data were collected using the Spectralis Spectral Domain-OCT (Heidelberg Engineering GmBH, Heidelberg, Germany), using the scanning protocol of the "Glaucoma module," which automatically centers

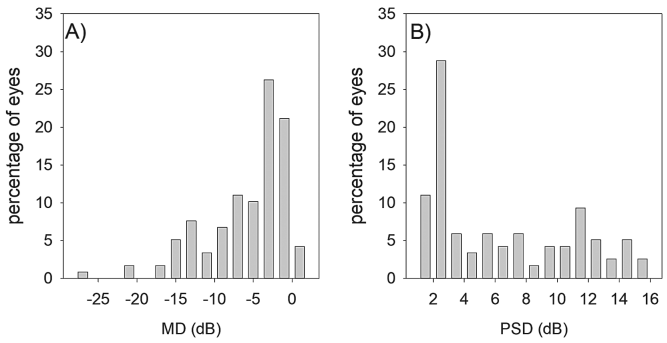


Figure 2. Histogram of the distribution of (**A**) mean deviation (MD) and (**B**) pattern standard deviation (PSD) in our dataset.

a series of three circular scans on the optic nerve head after detection of Bruch's membrane opening. For the analysis described herein, we selected the smallest of the three scan circles (3.5 mm diameter), which collect 768 A-scans in a 360° ring. The automated segmentation of the circumpapillary retinal nerve fiber layer (cpRNFL) was inspected and confirmed by a trained operator for all scans. All OCT data had signal strength above 20 dB. The cpRNFL data were exported after segmentation using proprietary tools (Heidelberg Engineering). Determination of the location of the optic nerve head relative to the fovea was enabled using proprietary tools, enabling extraction of coordinates of the fovea and Bruch's membrane opening identification from the Glaucoma module scanning protocol. The distribution of the position of the optic nerve head relative to the fovea in our dataset is shown in Figure 1B.

In addition to the cpRNFL data for 102 eyes, data were also available from a nominally vertical macular cube scan protocol designed to enable estimation of the position of the temporal raphe using the method of Bedggood et al.[20] The macular cube incorporated 49 B-scans collected across a 20°-square patch of retina, with the B-scans oriented perpendicularly to a line connecting the fovea to the center of the optic nerve head. For the 16 eyes for which vertical macular cube data were not available, the temporal raphe was assigned a value of 174°, which is a previously reported population average.[13] The distribution of data is shown in Figure 1C (note this includes the aforementioned 16 eyes).

Population-Based Map

The population-based map used in this study is that described by Jansonius et al.[9] Their method has an equation that returns the angle of a location on the retina that is a given distance from the center of the optic nerve head (polar coordinates) and whose axon

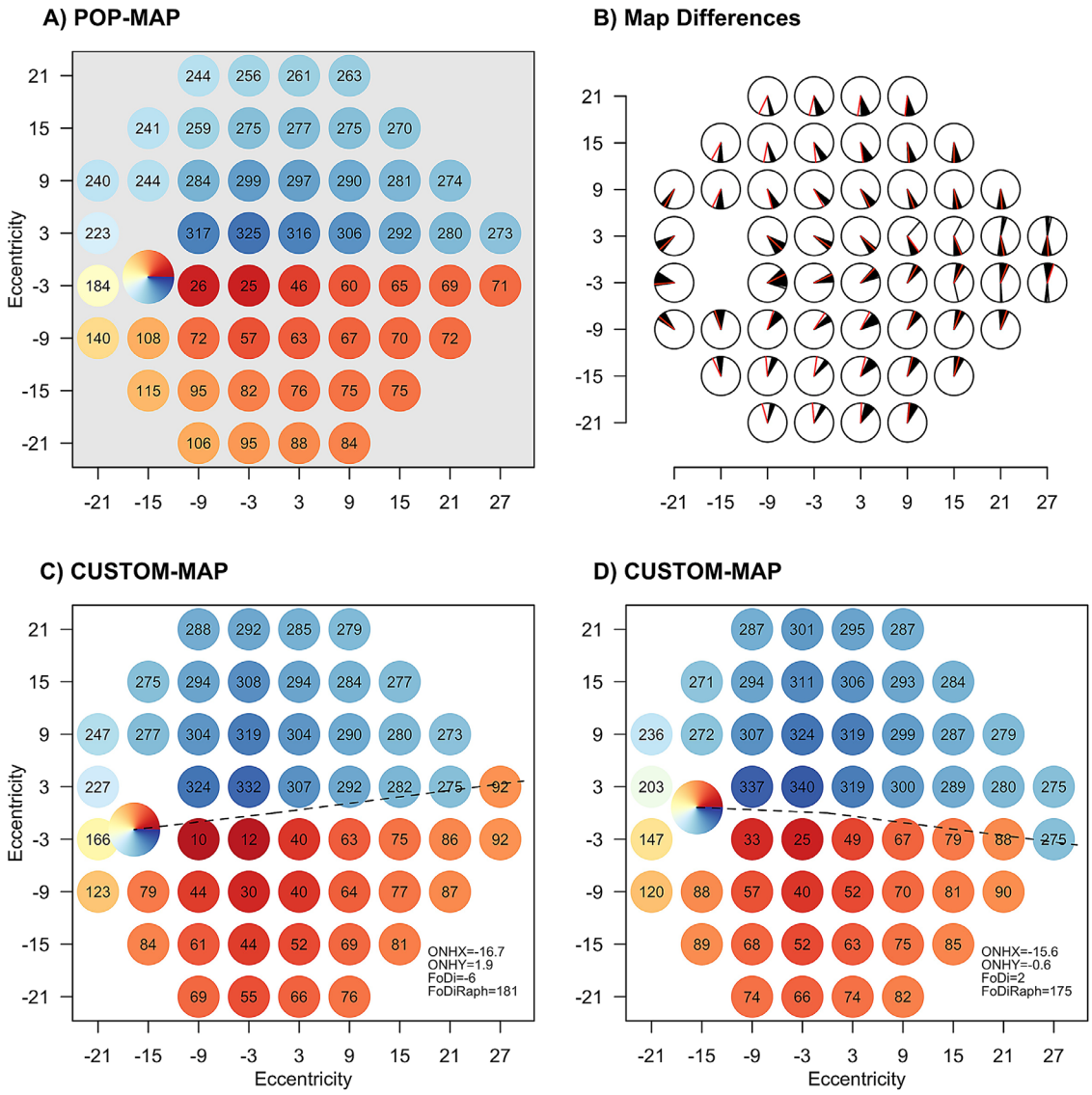


Figure 3. (**A**) The population map used in this study (the map of Jansonius et al.,[9] with correction of macular locations for Henle fiber length). Within each visual field location, the number responds to the angle of relevance on the optic nerve head with the convention that 0° is temporal, 90° is superior, 180° is nasal, and 270° is inferior. (**C** and **D**) Examples of individualized maps for two different eyes with the various anatomic landmarks of relevance from Figure 1 illustrated. (**B**) A *black line* for each eye in this study and a *red line* for POP-MAP show the angle where they map to the optic nerve head for each location in the VF.

crosses the edge of the optic nerve head at a given angle. To use this equation to generate a map of visual field locations to optic nerve head insertion angles requires two steps. The first is to map visual field locations onto corresponding retinal locations allowing for the displacement of photoreceptors and their associated ganglion cells. For this we use Figure 6 of Drasdo et al.[21] The second step, given the retinal location, is to search through all possible optic nerve head insertion points to find one that best fits the equation of Jansonius et al.[8,9] For this step, we assumed an optic nerve head of radius 3° and checked all angles in steps of 1°. The resulting map from 24-2 visual field locations to angles of insertion to the optic nerve head is shown in Figure 3A. This map is the same for all eyes and will be referred to as POP-MAP (abbreviation of "Population Map") throughout the remainder of the article.

The Individualized Map

Our model has three key differences relative to population average schema. The first of these is that the position of the optic nerve head relative to the fovea

is incorporated on an individual basis. The vertical position of the optic nerve head on the retina can vary from approximately 15° above through to 5° below the foveal position,[13,15,22] so intuitively it seems that this position would affect the angle of insertion of axons from fixed visual field locations into the optic nerve head.[16] Similarly the horizontal position of the optic nerve head will most likely make a difference to the angle of insertion of axons originating at visual field locations above and below the blind spot.

The second key difference between our approach and population average maps is that we allow the incorporation of variations in the position of the temporal raphe. Recent studies have shown that the angle of the raphe varies widely in individuals and is not reliably predicted by obvious retinal landmarks like position of the optic nerve head relative to the fovea.[13] Given the importance of the raphe for dividing superior and inferior visual field space, accommodating raphe angle variances within structure-function mapping should allow better reconciliation of functional and structural data in some patients. For example, we have previously argued, using data from the Beijing Eye Study, that around 12% of people are predicted to have "flipped" locations in the nasal step region; that is, visual field locations where the relevant pole of the optic nerve head is opposite to the population average.[10] Tanabe et al.[12] demonstrated that even greater percentages of people are likely to have an inverted structure-function relationship in the nasal region of the 10-2 visual field.

The third key difference between our computationally derived map and those derived from hand-tracing retinal nerve fiber bundle trajectories on retinal photographs[8,9] is our assumption that axons will travel the shortest possible path to the optic nerve head but avoid the foveal area.[16,17] This assumption results in straighter trajectories of retinal nerve fiber bundles that originate from retinal ganglion cells in the nasal retina. At face value, it is appealing to assume that hand-tracing photographs should define accurate trajectories because the retinal nerve fiber bundles can be directly visualized; however, this assumption could be false. The bundles that are visible in the nasal area of retinal photographs could be long bundles originating from retinal ganglion cells in the temporal retina that overlay bundles originating in the nasal retina. Similarly, tracing the trajectory of the complete absence of retinal nerve fiber bundles does not permit the pathways of axon bundles from nasal and temporal retina that share a final entry point in the ONH to be established. The trajectory of deeper layers of axons that are derived from retinal ganglion cells closer to the optic nerve head is difficult to confirm using current technology.

On the basis of these three principles, our map is derived using the following five rules:

1. Retinal ganglion cell axons arrive at the optic nerve head in order of distance from the optic nerve head, with closest retinal ganglion cells having their axons reach the optic nerve head before retinal ganglion cells further out in the retina.
2. Axons will attempt to follow the shortest path from their retinal ganglion cell body to the optic nerve head.
3. When arriving at the optic nerve head, if there is no room in the 1° sector at which the axon has arrived (by following the shortest path), then it is "bumped" to a sector that has room.
4. Axons are bumped superiorly or inferiorly depending on the location of their originating ganglion cell: temporal retina, above or below the temporal raphe; nasal retinal between fovea and the optic nerve head, above or below a line connecting the fovea and the optic nerve head center; and nasal retinal ganglion cells beyond the optic nerve head, above or below the horizontal.
5. Axons originating in the temporal retina are actively prevented from entering the optic nerve head in the papillomacular area.

This model of growth requires several parameters: the position of the optic nerve head relative to the fovea; the size of the optic nerve head; the radius of the fovea; the position of the temporal raphe; and a budget of the total number of axons that are allowed into each 1° sector. Here we assume the optic nerve head is a vertical ellipse with major axis 1.8 mm and minor axis 1.6 mm,[23] and the fovea is a circle with radius 0.67° of visual angle.[24,25] Also required for the model is an estimation of the number of retinal ganglion cells across the retina. For this purpose we use the data of Curcio and Allen[26] and assume the eye is a sphere matching their assumptions so that retinal ganglion cell density does not have to be scaled with axial length. To project parameters that are in degrees of visual angle onto the surface of this sphere, we assumed an axial length of 24.385 mm and a nodal length of 17.185 mm, which is the Gullstrand schematic model eye as assumed by the Spectralis for its calculations. To set the budget of allowed axons for each 1° sector of the optic nerve head we apportion 1.4 million[26] axons according to the sector areas of the assumed optic nerve head ellipse.

A final addition to the model since its original inception[17] is inclusion of the displacement of macular visual field locations from their ganglion cell bodies.

Consistent with our approach used for the derivation of a map from the Jansonius et al. equation, we use Figure 6 of Drasdo et al.[21] This does not alter the model per se, but it alters where one looks for a retinal ganglion cell, hence, axon insertion point for each visual field location.

Anatomic features for each eye in our empirical dataset were input to the model to derive an individualized map. Even though each map is potentially different for each eye, we will refer to these maps collectively as CUSTOM-MAP throughout the remainder of the article. Examples of CUSTOM-MAP derived for eyes with differing anatomic features are shown in Figure 3. An interactive version of the map for a subset of parameters is available[27] at https://people.eng.unimelb.edu.au/aturpin/sfMap.

Comparing Maps

We chose to compare CUSTOM-MAP and POP-MAP using structure-function concordance in the data. The obvious temptation is to compute structure-function correlations as are often reported in the literature[28–30] with each map and see which is higher. But to compare whether a visual field location is mapped to a feasible optic nerve head location based on one or other map in our cross-sectional data, we need to think carefully about what is reasonable to expect in the data.

If we assume that there is a direct (but unknown) relationship between cpRNFL loss and dB measured in the visual field, what could we observe in the clinical data we have? First, note that a visual field location from within the central 30° of visual field that is "healthy" could feasibly map to either a damaged or normal area on the optic nerve head. This is because axons inserting into the ONH can come from outside the central retina, and so it is feasible that peripheral axons are missing at the optic nerve head (causing a reduction in the OCT measurement) while the central visual field is intact. Examining whether normal visual field locations map to normal OCT areas in one map but not another gives us no information about whether one map is better than another. Thus we exclude normal visual field locations in our analysis (conservatively classified herein as total deviation > -6 dB). A related observation is that there is no guarantee that damage evident in the OCT will appear in the central visual field (because it may arise from damage to axons that represent the more peripheral visual field). Hence, we also cannot elicit differences in maps by using OCT as the reference for damage and seeing if visual field damage arises in one map and not the other. There is only one relationship between visual field and OCT that we can reliably expect to show a difference in maps: a damaged central visual field point should map to damage on the OCT.

The second factor driving our analytical approach is that while we are assuming that a damaged visual field location should correspond to a damaged OCT area (but not necessarily vice versa), there is no precise quantitative relationship between changes in visual field measurements and cpRNFL thickness measurements that is confirmed and established. Various models have been fit to databases of visual field sensitivity and cpRNFL to describe the average trends,[31,32] but there are wide confidence limits around these

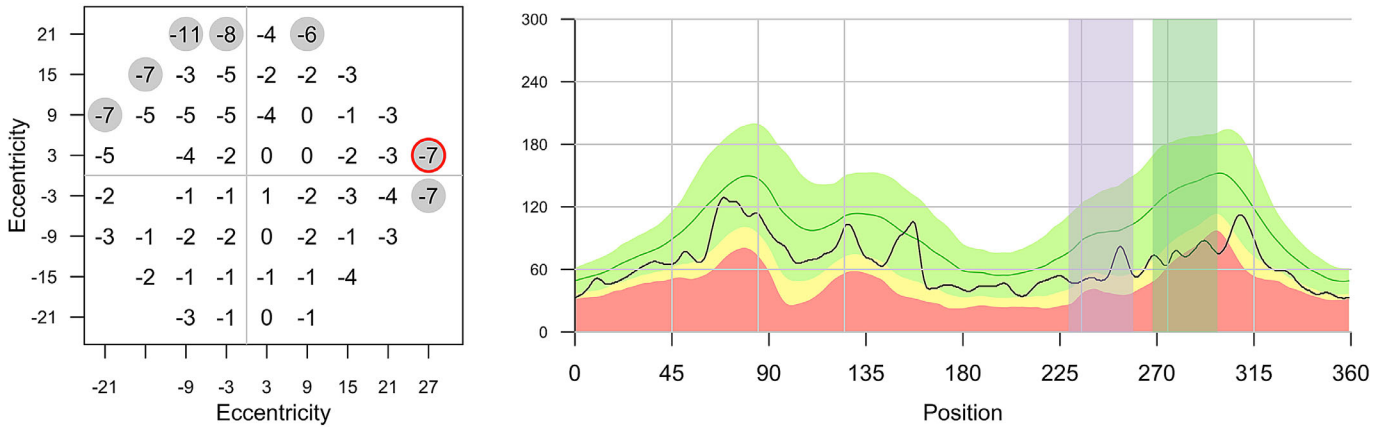


Figure 4. An example of structure-function concordance between a 24-2 visual field on the *left* (damaged locations shaded) and cpRNFL thickness on the *right*. For the circled, damaged visual field location, there is concordance for CUSTOM-MAP as the minimum cpRNFL thickness within ±15° of the mapped angle on the optic nerve head (*green shaded area*) is below 1% of normal, but not for POP-MAP (purple shaded area). In this eye with seven damaged visual field locations, the concordance ratio for CUSTOM-MAP is 57% (4/7) and 14% for POP-MAP (1/7).

models. Hence, we cannot estimate with tight precision what exact reduction in cpRNFL percentile one would expect for a reduction of 1 dB in total deviation in the visual field.

Given these limitations, we do not attempt model-based numerical correlations but count structure-function concordances within each eye. For this analysis, we define a concordance as when a visual field location has a sensitivity ≤ -6 dB from the normal average (a total deviation that is outside the expected normative range as defined above) and the cpRNFL thickness at the mapped location $\pm 15°$ on the optic nerve head is below the bottom 1% of the population values (modeled as a normal distribution using means and standard deviations from the Heidelberg Engineering US Mixed database as available for the Spectralis OCT). We chose a mapping region of $\pm 15°$ on the optic nerve head because our prior work exploring measurement variability in the fovea-ONH distance and angle with OCT suggests this to be an appropriate sector size.[33] The choice of cpRNFL thickness in the bottom 1% of population norms is a conservative choice; however, we explore varying this parameter later in the article. We define the number of concordances in an eye divided by the total number of damaged visual field locations as the *concordance ratio*. An example is shown in Figure 4. We then compare the concordance ratio for each eye using different mapping schemes.

Results

Figure 5 shows the difference in concordance ratio when using either mapping scheme. Eyes falling on the black line have the same concordance ratio using either mapping scheme. As can be seen by the sunflowers in the figure, there are numerous eyes where damaged visual field locations do not map to damaged OCT sectors for either mapping scheme (concordance ratio is 0) and also numerous eyes where all damaged locations map to damaged OCT sectors for both (concordance ratio is 1). The average concordance ratio over all eyes is higher using CUSTOM-MAP (0.605 c.f. 0.570, paired Wilcoxon test $P = 0.005$) but actually higher in 43 of 118 eyes, and POP-MAP has a higher ratio in 21 eyes. This suggests that the CUSTOM-MAP does offer advantages over POP-MAP on average for individual eyes.

An alternate view of the differences is given in Figure 6 where concordance is now broken out for each spatial location in the 24-2 pattern, rather than computed as a single ratio for each eye. Panel A of Figure 6 uses the same strict criterion for concordance as described above. For example, in location (15 degrees, 15 degrees) of Panel A, of the 45 eyes that have a visual field deficit (total deviation < -5 dB), 34 eyes have concordance (the mapped location on the optic nerve head has cpRNFL thickness less than 1%

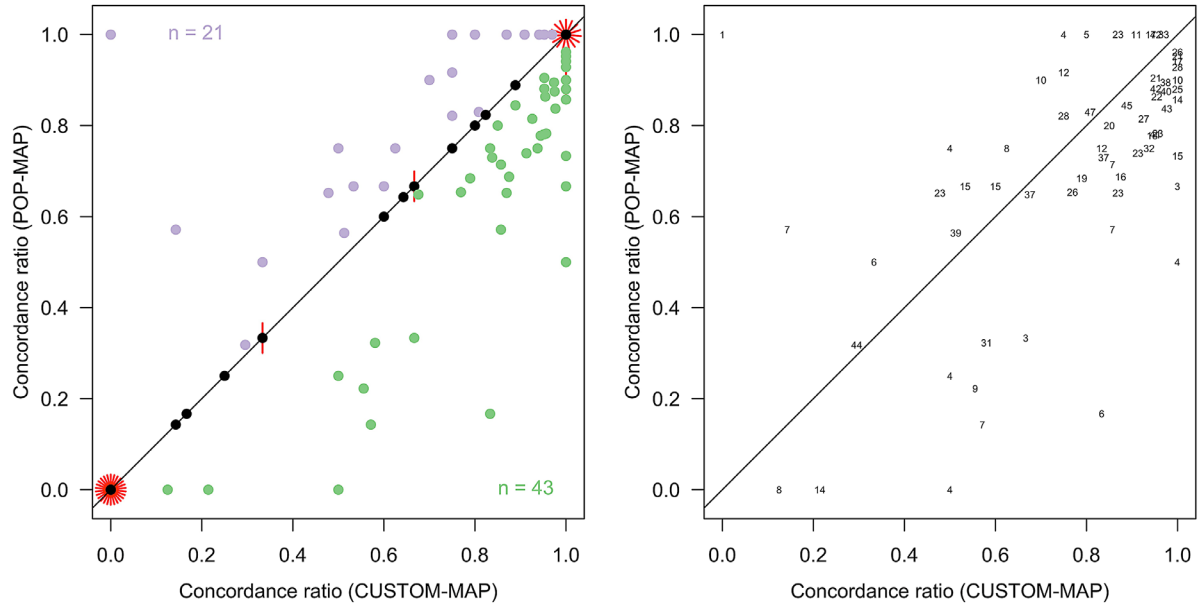


Figure 5. Difference in concordance ratio when using CUSTOM-MAP vs POP-MAP for each eye. The *left panel* shows one dot per eye, with *red stalks* showing a count of eyes that share ratios (a Sunflower plot). *Purple dots* indicate those eyes where POP-MAP has a higher ratio (21 eyes), and *green* the converse (43 eyes). The *right panel* shows the same data, but each symbol gives the number of damaged visual field locations (total deviation < -5 dB) for those eyes where the concordance ratio differed.

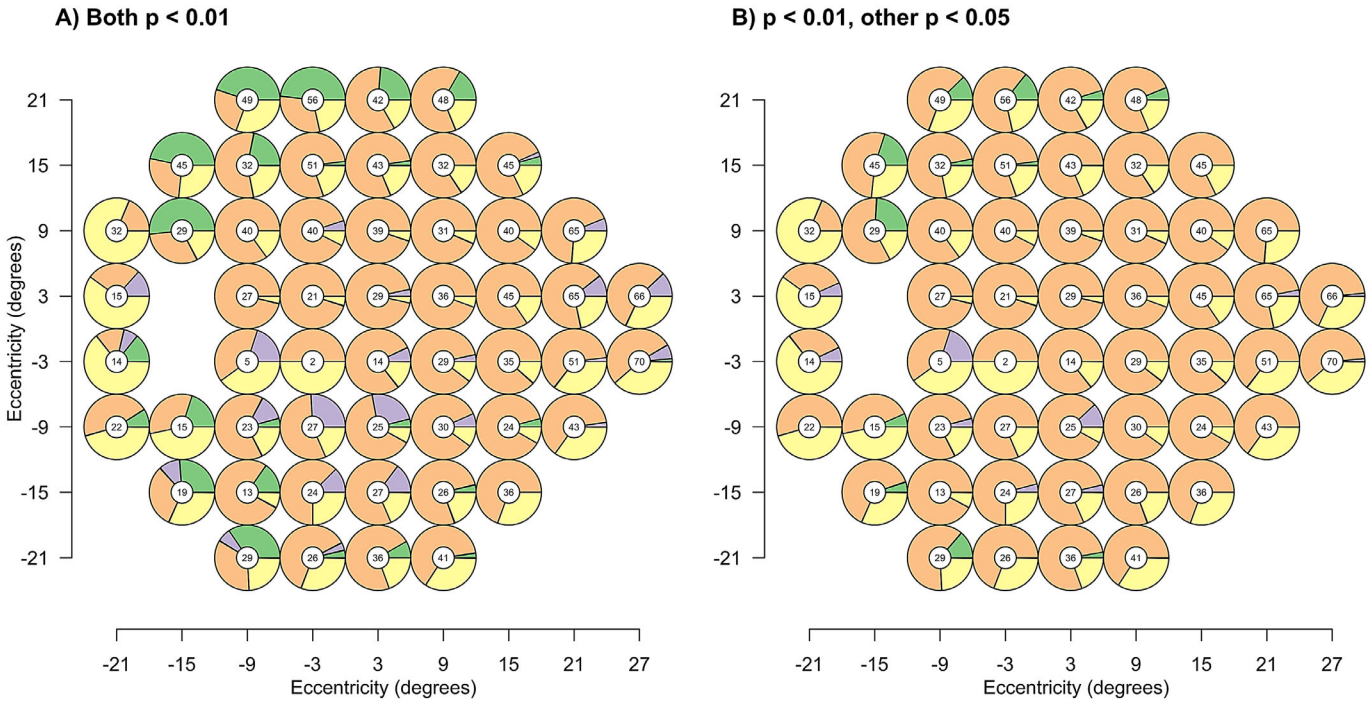


Figure 6. Each pie shows the proportion of eyes that have concordance at each location for: CUSTOM-MAP only (*green*); POP-MAP only (*purple*); both CUSTOM-MAP and POP-MAP (*orange*); and neither maps (*yellow*). The number in the middle of each location is the number of eyes with total deviation < -5 dB at that location. (**A**) The situation where agreement between the two mapping schema requires both to match to an area of cpRNFL thickness <1% of normal. (**B**) The situation where agreement is relaxed such that one map must be cpRNFL thickness <1% of normal with the other being cpRNFL thickness <5% of normal.

of normal) using both maps, one eye has concordance using POP-MAP but not CUSTOM-MAP (purple), two eyes have concordance using CUSTOM-MAP but not POP-MAP (green), and eight eyes do not have concordance with either map (yellow).

If we take concordance as a measure of accuracy of the mapping approach, at first glance it appears that the CUSTOM-MAP is better than POP-MAP around the peripheral temporal field (more green), and the reverse is true in the inferior macular region (more purple). On closer inspection, however, many of the definitive "wins" for either method (the green and purple) result from the strict percentile boundary of 1% in the cpRNFL thickness for concordance with the visual field damage. In particular, there are many cpRNFL thicknesses of 2% or 3% of normal that appear in the mapped regions for both methods that are not classified as concordance but clinically would most likely be interpreted as a concordance. To investigate the effect of this boundary condition, we keep the strict requirement that one mapping approach must map a damaged visual field location to an area of cpRNFL thickness that is <1% of normal to concord, but for this to be unique concordance for this mapping approach, the other map should indicate an area that is above some higher percentile of normal. In panel B of Figure 6, this higher percentile is 5%. That is, one map must have an area of cpRNFL thickness that is < 1% of normal concordant with a visual field defect, and the other map can have a concordant area of cpRNFL thickness that is <5% of normal and still be classified as agreement in mapping. As expected, this removes some of the "wins" for each method (less purple and green).

Figure 7 shows the effect of this relaxation for various values of percentile. The first point on each curve has the requirement that both maps must indicate cpRNFL thickness <1% for each damaged visual field point to concord, which is the criteria used to generate Figure 6A. A total of 148 locations concord for CUSTOM-MAP alone (the sum of all of the green sectors in Fig. 6), and 66 for POP-MAP alone (the sum of all of the purple sectors in Fig. 6). If we relax the requirement for POP-MAP to concord to 10% of normal cpRNFL thickness, but keep CUSTOM-MAP at 1%, we see that the number of locations that concord when using CUSTOM-MAP but not when using POP-MAP (the "C" curve) falls to 27 locations.

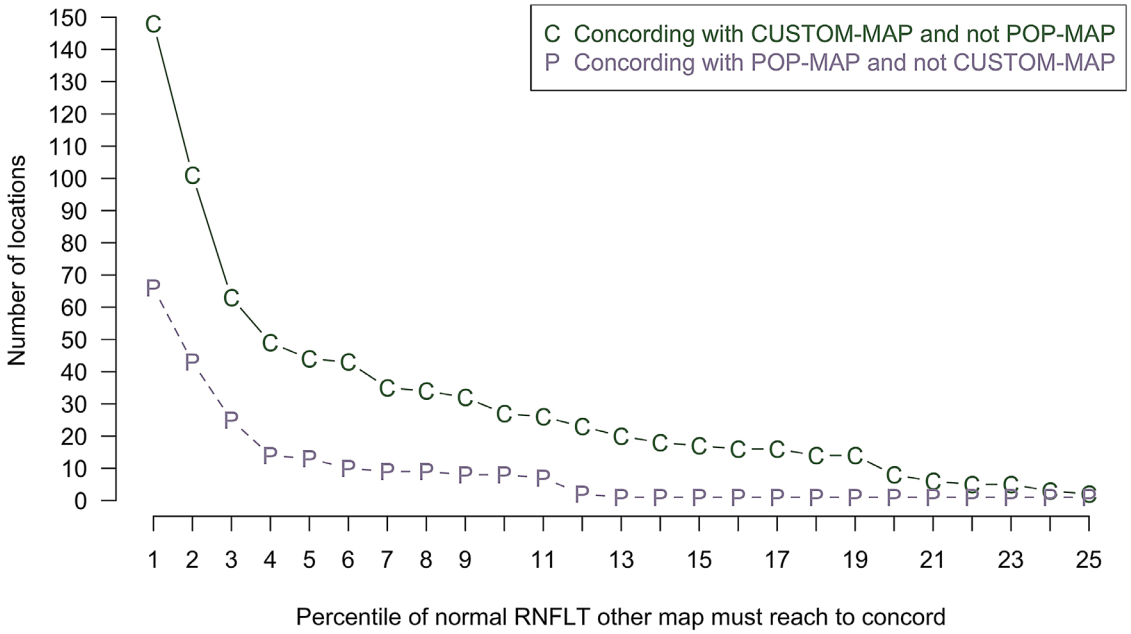


Figure 7. Number of locations that concord using one map and not the other when the first map has a requirement of <1% of normal for cpRNFL thickness, and the other map has a requirement given on the x-axis. As the requirement on the second map is relaxed, more locations concord using both mapping schemes, so the total number of one or the other decreases.

Similarly, if we do the reverse, the number of locations that concord using POP-MAP alone falls to eight. This demonstrates that there are quite a number of "wins" for each mapping technique that are very close to the boundary condition of 1% of normal. Even relaxing the criteria so that the other map can be 5% or less reduces the number of "wins" shown in Figure 6 from 148 to 44 for CUSTOM-MAP and from 66 to 13 for POP-MAP.

Given this boundary effect, to more accurately examine the spatial differences in the two maps, as measured by concordance, we replot Figure 6 using a generous cutoff of classifying abnormality where cpRNFL thickness has a probability of less than 1% for one of the maps, and 10% for the alternate map as shown in Figure 8. We use this quite liberal cutoff to identify areas where there are quite profound differences in mapping predictions. This figure also includes the relevant sections of the OCT profiles as panels around the outside, which show the cpRNFL thickness for the eyes where one map concords and the other does not. It does appear here that CUSTOM-MAP is better in the superior temporal field, whereas POP-MAP has some gains in the inferior macular region. Note, for many locations, with this relaxed criterion (relative to Fig. 6) there are many more eyes where both CUSTOM-MAP and POP-MAP agree (orange and yellow sectors).

Discussion

When we initially conceived our individualized structure-function mapping approach, some relevant features of interest were not readily available in empirical datasets, hence prior comparisons with other mapping schema have been performed using simulation. Several features key to the model are now either routinely available outcomes from clinical OCT (the position of the optic nerve head relative to the fovea), or are readily measurable (temporal raphe). This is the first study to directly compare mapping schema using such an empirical dataset. On average, for the dataset used herein, the CUSTOM-MAP has benefits in some eyes, and demonstrates on average better concordance between structure and function than the POP-MAP approach. In particular in the arcuate regions, CUSTOM-MAP was more likely than POP-MAP to match with damaged OCT (Fig. 6, green wedges), however, POP-MAP matched better with OCT damage in the inferior macular region (Fig. 6, purple wedges).

Modeling studies can act as a driver to find empirical support to either prove or disprove assumptions of the model. For example, in our first detailed exploration of our CUSTOM-mapping model, our assumptions regarding the temporal raphe positioning were incorrect (we assumed continuation of the FoDi line). Subsequently, high-resolution transverse section OCT

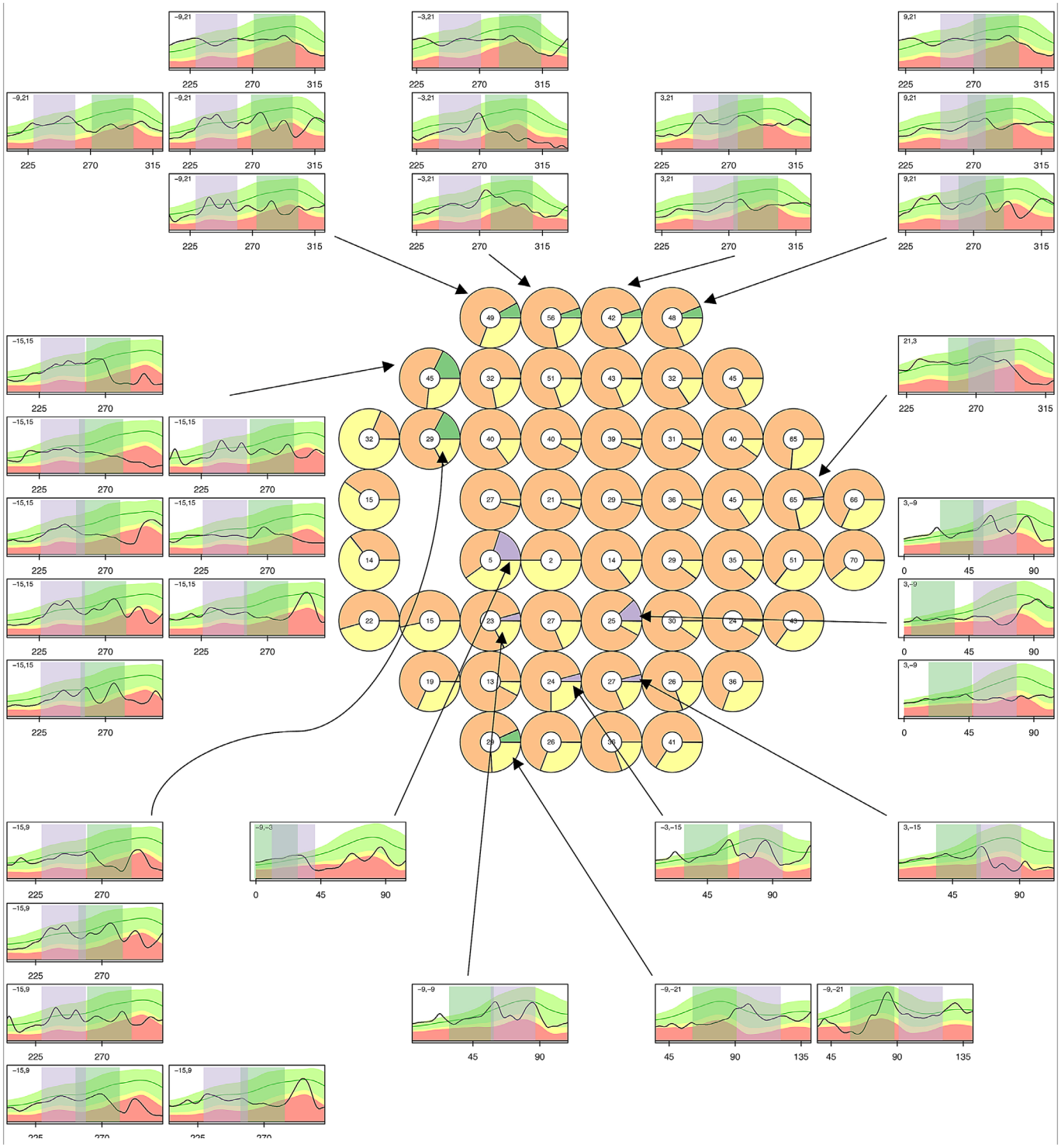


Figure 8. The central 24-2 graphic is as in Figure 6, with the segments of OCT plots around the edge given for each case where one mapping schema appeared to "win." *Green shading* in the central plot indicates the number of eyes for which the corresponding location maps to a cpRNFL thickness $< 1\%$ for CUSTOM-MAP and cpRNFL thickness$> 10\%$ for POP-MAP; *purple shading* shows the reverse; *yellow* indicates the number of eyes where neither map has cpRNFL thickness$< 1\%$, and *orange* shows the remaining eyes. The number in the middle of each location is the total number of eyes with total deviation < -5 dB at that location. For the surrounding OCT plots, *green vertical shading* shows the area indicated by CUSTOM-MAP, and *purple* POP-MAP.

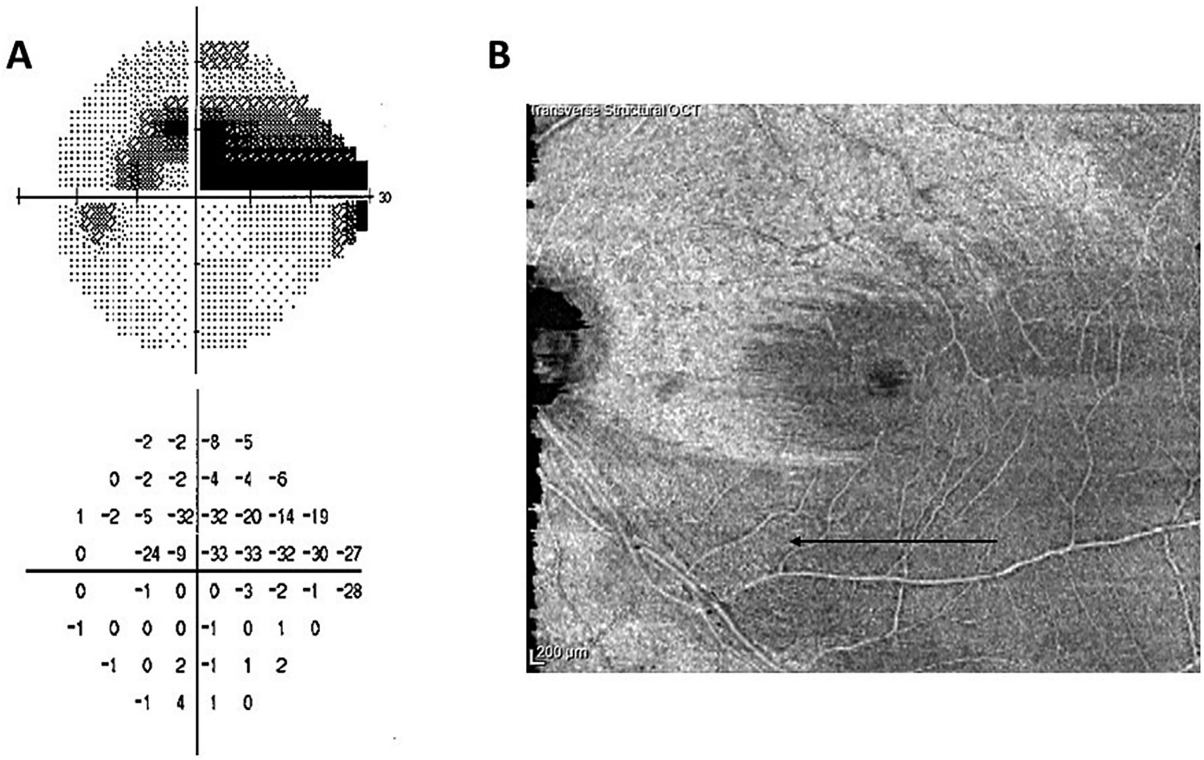


Figure 9. Case example consistent with the possibility of "straighter" retinal nerve fiber bundle trajectories for deeper retinal nerve fiber layers. (**A**) The visual field data (*top panel* is gray-scale from HFA 24-2 SITA Standard, *bottom panel* is TD) corresponding to the en-face OCT shown in Panel B. (**B**) A high-resolution transverse section at 21 µm below the inner limiting membrane with a sharpening filter applied (Imagemagick[36] -sharpen 0 × 4).

imaging of the raphe have enabled this assumption to be corrected,[11,13,34] and we have refined both the model and knowledge of population variance of this anatomic feature.

A key feature of our current model that similarly may deserve empirical investigation is the assumption that axons between the fovea and disc take a direct, straight path into the optic nerve head (rather than a longer curvilinear path). These straighter trajectories largely drive the differences between CUSTOM-map and POP-map in the superior and inferior visual field regions between the optic nerve head and the macula. In this superior visual field, CUSTOM-map appeared to show advantages over POP-map in some eyes (Fig. 6). The straight path model arises from the intuition that axons would take the shortest possible path to the optic nerve head during development. There is no clear physical reason for these bundles to follow curved trajectories to avoid the fovea like their temporal counterparts. However, bundles in this area may fasciculate with temporal bundles and follow their curved path. Visualization of reflective surface bundles in retinal photography cannot help to answer this question, because photos do not allow visualization of trajectories below the retinal surface. Straighter overlapping retinal nerve trajectories have been reported in some eyes when there are RNFL defects in retinal photos[35]; however, accurate understanding of the positioning of the trajectories in the Z-plane is difficult in the 2D image. Visualization of bundle trajectories in different depth planes may now be visible with high-resolution en-face OCT in select eyes with particular patterns of arcuate damage.

Figure 9 shows a case example of an eye with extensive inferotemporal retinal nerve fiber layer drop-out. The high-resolution OCT scan (Spectralis, 30 × 25°, 241 horizontal B-scans, 30 µm separation, ART 16) is shown en face at 21 µm below the inner-limiting membrane. In the superior retina, trajectories of the bundles appear curvilinear; however, the large amount of reflectile bundle tissue is problematic for visualization of bundles at different depths. Simply sectioning the OCT data en face at slight differences in depths through healthy tissue does not solve this problem. Inferiorly, because of the absence of surface bundles, a wedge of deeper bundles are visible entering the optic nerve head. These appear to be straighter in profile, suggesting that the trajectory of RNFL bundles may indeed differ in different depth planes. Clearly, a larger dataset of

high-resolution en-face images in eyes with localized retinal nerve fiber bundle defects is required to explore this systematically; however, this case example is suggestive of differences in nerve fiber trajectories at different depth planes. Interestingly, previous reports of straighter fibers visualized in occasional retinal photos have also been in the inferior temporal retina.[36] Perhaps there is an anatomic asymmetry in the bundle trajectories between the superior and inferior retina that might contribute to the trend for POP-MAP to show some advantages over CUSTOM-MAP in the inferotemporal macular region of the visual field in a limited number of eyes (purple sectors in Fig. 6A). Future high-resolution OCT imaging may assist in resolving these questions.

In choosing our analytical approach, we considered very carefully assumptions that are implicit in various presentations of structure-function relationships and settled on using a simple approach to validate point-wise concordance between visual field and OCT outcomes. In addition to the assumptions discussed, this type of approach shares similarities to that used by eye clinically. In addition to comparing mapping, there are other structure-function analyses and potential applications for which this type of concordance approach may be suitable, for example, if we simply wanted to direct the sampling of visual field testing into regions of interest that are spatially concordant with retinal nerve fiber layer damage.[37] However, a more quantitative approach that estimates the likely depth of visual field damage for a measured retinal nerve fiber layer thickness decrease is necessary if visual field algorithms are to seeded with more efficient starting estimates predicted from retinal nerve fiber layer damage,[1,2] or if structural data were to be used to predict the visual field.[38] We contest that for these approaches to have maximal benefit for individual eyes, a CUSTOM-MAP approach is warranted. It may also be the case that through the use of CUSTOM-MAP, in addition to other approaches to decrease noise in both OCT and visual field estimates, better models to enable quantitative prediction between OCT and visual field could be derived.

Here we defined a visual field defect as a total deviation of less than or equal to 6 dB. Our study inclusion criteria removed individuals with significant lens opacity, required all individuals to have reasonable visual acuity, and required the visual field defect to have a spatial pattern consistent with glaucoma. Consequently, we consider it unlikely that the visual field data is significantly contaminated by nonglaucomatous lesions (however, it may be contaminated by measurement noise). Importantly, because we are comparing the two mapping schema on the same visual field locations, any visual field location that was classified as defective but where the defect arose as a result of a reason other than glaucoma, should potentially be nonconcordant with cpRNFL thinning for both schema. For more general usage of the concordance approach for matching structural and functional damage, there may be advantages to using pattern deviation metrics to minimize potential contamination of the classification of visual field locations due to issues that affect the general height of the visual field.

To perform this analysis, we required a database of visual fields and OCT images that had estimates of the temporal raphe, in addition to the FoDi angle (angle between the fovea and the optic nerve head as illustrated in Fig. 1A). Estimation of the FoDi is now commonplace in commercially available OCT. The temporal raphe can be visualized with improved precision with higher resolution scans. With rapidly increasing OCT scanning speeds, incorporating such measurements as standard in commercial "glaucoma" OCT protocols may be feasible. There are already automated approaches for detecting the raphe,[20,39] and information regarding changes to the apparent position, width, or reflectance of the raphe may provide useful, additional information for glaucoma management.[39,40] We have previously shown that the distribution of raphe positions is similar in those with glaucoma to age-matched controls[13]; however, we are unaware of any literature describing substantial longitudinal follow-up of the raphe architecture in glaucoma. With more advanced disease, as the retinal nerve fiber bundles are lost in the raphe region, the precision of measurement of raphe position is expected to decrease. In the context of our mapping, if it is assumed that the position of remaining retinal ganglion cell bodies stays relatively fixed in the retina, then using a raphe position measured earlier in the disease process for an individual would seem appropriate.

Another recent advance in commercially available OCT for glaucoma is wide-field imaging. In this article we have concentrated analysis on cpRNFL scans because cpRNFL data is widely used in practice and has extensive normative data in a range of commercial instruments. Structure-function mapping for wide-field imaging can be performed largely by direct superimposition on wide-field imaging, if the region of interest in the OCT is the region immediately stimulated by the perimetric stimulus (with some correction in the macular region for Henle fiber displacement as described in the methods). However, any analysis that relates optic nerve head, Bruch's membrane opening, or cpRNFL data to the visual field will require mapping schema similar to ours

(or previously published approaches). Our mapping schema is also relevant to retinal photography for environments where OCT is still an expensive and not-so-accessible technology.

It is worth noting that there are other individual anatomic factors that could be customized within the model but that we chose to keep as population estimates. One example is disc size in the horizontal and vertical direction. In the model there is an interplay between retinal ganglion cell density and disc size. For example, if the disc is made longer in the vertical direction, but the number of RGCs kept the same, then locations in the nasal field will have higher angles of insertion into the optic nerve head (toward "poles") because the budget of allowable axons into the optic nerve head around the horizontal meridian is decreased and those at "the poles" is increased. Because we do not know how the total number of retinal ganglion cells relates to disc size and shape (if at all) in the population, we have chosen to avoid this complication and instead to use a population average for disc shape[23] and number of retinal ganglion cells.[26] We also chose to use a population average value for the foveal radius.[24,25] Our previous work on attempting to customize this value provided some benefit, but it was relatively limited.[41,42] Future comparisons of model performance in highly myopic eyes with glaucoma may reveal additional features such as disc tilt that may improve model performance. Our current dataset only included five eyes with myopia greater than −6D, which does not enable such analysis.

In summary, we present an updated model customized to an individual's eye that maps any location in the visual field to the optic nerve head, enabling structure-function analysis. This model allows individual maps to be derived based on a few, readily measurable anatomical features. Using an empirical database where data for these features was available, we demonstrate that the customized mapping approach results in improved concordance between structural and functional data in some eyes, when compared to a map based on population averages. We argue that structure-function mapping schema are best compared using a concordance approach. Our mapping schema is readily available for both clinical and research purposes.

Acknowledgments

OCT image in Figure 9 was supplied by Vasanth Muthusamy.

Disclosure: **A. Turpin,** Heidelberg Engineering GmBH (F); **A.M. McKendrick,** Heidelberg Engineering GmBH (F)

References

1. Denniss J, McKendrick AM, Turpin A. Towards patient-tailored perimetry: Automated perimetry can be improved by seeding procedures with patient-specific structural information. *Trans Vis Sci Tech*. 2013;2(4):3.
2. Ganeshrao SB, McKendrick AM, Denniss J, Turpin A. A Perimetric Test Procedure That Uses Structural Information. *Optom Vis Sci*. 2015;92:70–82.
3. Medeiros FA, Lisboa R, Weinreb RN, Girkin CA, Liebmann JM, Zangwill LM. A combined index of structure and function for staging glaucomatous damage. *Arch Ophthalmol*. 2012;130:1107–1116.
4. Swanson WH, Horner DG. Assessing assumptions of a combined structure-function index. *Ophthalmic Physiol Opt*. 2015;35:186–193.
5. Denniss J, Turpin A, McKendrick AM. Relating optical coherence tomography to visual fields in glaucoma: structure-function mapping, limitations and future applications. *Clinical Exp Optom*. 2019;102:291–299.
6. Garway-Heath DF, Holder GE, Fitzke FW, Hitchings RA. Relationship between electrophysiological, psychophysical, and anatomical measurements in glaucoma. *Invest Ophthalmol Vis Sci*. 2002;43:2213–2220.
7. Garway-Heath DF, Poinoosawmy D, Fitzke FW, Hitchings RA. Mapping the visual field to the optic disc in normal tension glaucoma eyes. *Ophthalmology*. 2000;107:1809–1815.
8. Jansonius NM, Nevalainen J, Selig B, et al. A mathematical description of nerve fiber bundle trajectories and their variability in the human retina. *Vision Res*. 2009;49:2157–2163.
9. Jansonius NM, Schiefer J, Nevalainen J, Paetzold J, Schiefer U. A mathematical model for describing the retinal nerve fiber bundle trajectories in the human eye: Average course, variability, and influence of refraction, optic disc size and optic disc position. *Exp Eye Res*. 2012;105:70–78.
10. McKendrick AM, Denniss J, Wang YX, Jonas JB, Turpin A. The proportion of individuals likely to benefit from customized optic nerve head structure-function mapping. *Ophthalmology*. 2017;124:554–561.
11. Chauhan BC, Sharpe GA, Hutchinson DM. Imaging of the temporal raphe with optical

coherence tomography. *Ophthalmology*. 2014;121: 2287–2288.
12. Tanabe F, Matsumoto C, McKendrick AM, Okuyama S, Hashimoto S, Shimomura Y. The interpretation of results of 10-2 visual fields should consider individual variability in the position of the optic disc and temporal raphe. . *Br J Ophthalmol*. 2017;102:323–328.
13. Bedggood P, Nguyen BN, Lakkis G, Turpin A, McKendrick AM. Orientation of the temporal nerve fiber raphe in healthy and in glaucomatous eyes. *Invest Ophthalmol Vis Sci*. 2017;58:4211–4217.
14. Huang G, Gast TJ, Burns SA. In vivo adaptive optics imaging of the temporal raphe and its relationship to the optic disc and fovea in the human retina. *Invest Ophthalmol Vis Sci*. 2014;55:5962–5961.
15. Chauhan BC, Burgoyne CF. From clinical examination of the optic disc to clinical assessment of the optic nerve head: A paradigm change. *Am J Ophthalmol*. 2013;156:218–227.
16. Denniss J, McKendrick AM, Turpin A. An anatomically customizable computational model relating the visual field to the optic nerve head in individual eyes. *Invest Ophthalmol Vis Sci*. 2012;53:6981–6990.
17. Turpin A, Sampson GP, McKendrick AM. Combining ganglion cell topology and data of patients with glaucoma to determine a structure-function map. *Invest Ophthalmol Vis Sci*. 2009;50:3249–3256.
18. Carreras FJ, Medina J, Ruiz-Lozano M, Carreras I, Castro JL. Virtual tissue engineering and optic pathways: plotting the course of the axons in the retinal nerve fiber layer. *Invest Ophthalmol Vis Sci*. 2014;55:3107–3119.
19. Chylack LTJ, Wolfe JK, Singer DM, et al. The Lens Opacities Classification System III. The Longitudinal Study of Cataract Study Group. *Arch Ophthalmol*. 1993;111:831–836.
20. Bedggood P, Tanabe F, McKendrick AM, Turpin A. Automatic identification of the temporal retinal nerve fiber raphe from macular cube data. *Biomed Opt Exp*. 2016;7:4043–4053.
21. Drasdo N, Millican CL, Katholi CR, Curcio CA. The length of Henle fibers in the human retina and a model of ganglion receptive field density in the visual field. *Vision Res*. 2007;47:2901–2911.
22. Jonas RA, Wang YX, Yang H, et al. Optic disc – fovea angle: The Beijing Eye Study 2011. *PLoS One*. 2015;10:e0141771.
23. Quigley HA, Brown AE, Morrison JD, Drance SM. The size and shape of the optic disc in normal human eyes. *Arch Ophthalmol*. 1990;108: 51–57.
24. Hendrickson AE, Youdelis C. The morphological development of the human fovea. *Ophthalmology*. 1984;91:603–612.
25. Yamada E. Some structural features of the fovea centralis in the human retina. *Arch Ophthalmol*. 1969;82:151–159.
26. Curcio CA, Allen KA. Topography of ganglion cells in human retina. *J Comp Neurol*. 1990;300:5–25.
27. Turpin A, McKendrick AM. Updated customizable structure-function map from visual field to optic nerve head. *Invest Ophthalmol Vis Sci (ARVO Annual Meeting Abstract)*. 2019;60:6140.
28. Ganeshrao SB, Turpin A, Denniss J, McKendrick AM. Enhancing structure-function correlations in glaucoma with customized spatial mapping. *Ophthalmology*. 2015;122:1695–1705.
29. Gardiner SK, Johnson CA, Cioffi GA. Evaluation of the structure-function relationship in glaucoma. *Invest Ophthalmol Vis Sci*. 2005;46:3712–3717.
30. Bowd C, Zangwill LM, Medeiros FA, et al. Structure-function relationships using confocal scanning laser ophthalmoscopy, optical coherence tomography, and scanning laser polarimetry. *Invest Ophthalmol Vis Sci*. 2006;47:2889–2895.
31. Hood DC, Anderson SC, Wall M, Kardon RH. Structure versus function in glaucoma: an application of a linear model. *Invest Ophthalmol Vis Sci*. 2007;48:3662–3668.
32. Harwerth RS, Wheat JL, Fredette MJ, Anderson DR. Linking structure and function in glaucoma. *Prog Retin Eye Res*. 2010;29:249–271.
33. Denniss J, Turpin A, McKendrick AM. Individualized structure-function mapping for glaucoma: practical constraints on map resolution for clinical and research applications. *Invest Ophthalmol Vis Sci*. 2014;55:1985–1993.
34. Bedggood P, Mukherjee S, Nguyen BN, Turpin A, McKendrick AM. Geometry of the retinal nerve fibers from emmetropia through to high myopia at both the temporal raphe and optic nerve. *Invest Ophthalmol Vis Sci*. 2019;60:4896–4903.
35. Jeoung JW, Kim TW, Kang KB, Lee JJ, Park KH, Kim DM. Overlapping of retinal nerve fibers in the horizontal plane. *Invest Ophthalmol Vis Sci*. 2008;49:1753–1757.
36. Team TID. ImageMagick. Available at: https://imagemagickorg 2020. Accessed December 20, 2020.
37. Ganeshrao SB, Turpin A, McKendrick AM. Sampling the visual field based on individual retinal

nerve fiber layer thickness profile. *Invest Ophthalmol Vis Sci*. 2018;59:1066–1074.
38. Zhu H, Crabb DP, Fredette MJ, Anderson DR, Garway-Heath DF. Quantifying discordance between structure and function measurements in the clinical assessment of glaucoma. *Arch Ophthalmol*. 2011;129:1167–1174.
39. Ashimatey BS, King BJ, Malinovsky VE, Swanson WH. Novel technique for quantifying retinal nerve fiber bundle abnormality in the temporal raphe. *Optom Vis Sci*. 2018;95:309–317.
40. Huang G, Luo T, Gast TJ, Burns SA, Malinovsky VE, Swanson WH. Imaging glaucomatous damage across the temporal raphe. *Invest Ophthalmol Vis Sci*. 2015;56:3496–3504.
41. Sepulveda JA, Turpin A, McKendrick AM. Individual differences in foveal shape: feasibility of individual maps between structure and function within the macular region. *Invest Ophthalmol Vis Sci*. 2016;57:4772–4778.
42. Turpin A, Chen S, Sepulveda JA, McKendrick AM. Customising structure-function displacements in the macula for individual differences. *Invest Ophthalmol Vis Sci*. 2015;56:5984–5989.